

# Three-dimensional movable metamaterial using electric split-ring resonators

Yu-Sheng Lin, Fusheng Ma, and Chengkuo Lee\*

Department of Electrical & Computer Engineering, National University of Singapore, 4 Engineering Drive 3, 117576, Singapore

\*Corresponding author: elelc@nus.edu.sg

Received May 15, 2013; revised June 17, 2013; accepted July 19, 2013;

posted July 23, 2013 (Doc. ID 190653); published August 13, 2013

We have demonstrated a three-dimensional movable metamaterial (MM) with reconfigurable electric split-ring resonators (eSRR) at terahertz frequencies. This is accomplished by making planar arrays of eSRR with movable stress curved beams (eSRR-MSCBs) which are actuated out-of-plane by electrostatic force. Our results have demonstrated that the eSRR-MSCBs possess blueshifting capabilities and polarization dependent state at terahertz frequencies, while such adaptive MMs offer significant potential in realizing electromagnetic functionality with diversified applications, such as sensors, switches, and filters. © 2013 Optical Society of America

OCIS codes: (160.3918) Metamaterials; (260.5740) Resonance; (300.6495) Spectroscopy, terahertz.

<http://dx.doi.org/10.1364/OL.38.003126>

Recently, electromagnetic metamaterials (MMs) have attracted considerable interest owing to their potential applications, such as high-resolution superlenses, invisibility cloaking devices, and perfect absorbers [1–3]. The realization of such extraordinary optical properties relies on the properties of MMs to create independently tailored electric and magnetic responses to incident radiation. Moreover, a unique property of terahertz waves is that they transmit through most nonaqueous and non-metallic materials. Plenty of works on MMs have been performed in the terahertz frequency range and tunable terahertz MMs have also received significant attention because of their potential applications as MM devices [4].

Currently, tunability of MMs using different structures to realize negative refractive index properties have been demonstrated by various fabrication technologies and optimized designs [5–16]. With the aid of tunability, reconfigurable MM devices become feasible in many applications, such as sensors, switches, and filters [17]. Voltage variable capacitances have been generally used to achieve electronic tuning in resonators. Such variable capacitances, which contribute to the overall capacitance of the resonators, have been implemented by means of semiconductor diodes [5,6] or by changing the surrounding media [7–9]. These tuning methods are often used to adjust the resonant frequency, which is highly dependent on the nonlinear properties of the nature material. However, the tuning ranges in the terahertz frequency are only 0.07 and 0.15 THz by means of semiconductor diodes [5,6] and liquid crystal [8,9], respectively. These methods suffer from a limited tuning range as the variation of material properties of surrounding media is usually very small. Meanwhile, microelectromechanical systems (MEMS) technology has been well developed for the realization of three-dimensional (3D) movable micromechanical devices, hence providing an ideal platform to directly reconfigure unit cells [10–16]. MEMS-based MMs having bulk-micromachined unit cells demonstrate tunable characteristics because of variable in-plane gap [11–13]. This approach overcomes the limitations of changing MM composition.

In this Letter, we report a 3D movable MM and investigated its optical properties. Other than in-plane gap

tuning mechanism within the unit cells [11–13], we have also developed a tuning mechanism to actively control the MMs by changing the air gap between the metallic structures and the substrate. These 3D movable MMs were designed based on electric split-ring resonators with movable stress-curved beams (eSRR-MSCBs) and fabricated using surface micromachining. This fabrication process enables monolithic integration of tunable MMs with standard CMOS process.

Figure 1(a) shows the scanning electron microscopy (SEM) image of the eSRR array. The lattice parameters of an eSRR unit cell are indicated in Fig. 1(b). The lattice constants are 130  $\mu\text{m}$  along the  $x$  direction and 110  $\mu\text{m}$  along the  $y$  direction. The gaps and line width of each beam within the eSRR unit cell are 4  $\mu\text{m}$ . The area of a square unit cell is 88  $\mu\text{m} \times 88 \mu\text{m}$ . Surface micromachining is developed to demonstrate eSRR-MSCBs with out-of-plane motion capability as shown in Fig. 1(c). First,  $\text{SiO}_2$  thin film 100 nm thick was deposited and patterned on standard silicon wafer as an anchor for MSCBs. Second, an  $\text{Al}_2\text{O}_3$  thin film was deposited on surface by using atomic layer deposition 20 nm thick, and a stressed layer of Al was evaporated to 500 nm thick by *physical vapor deposition*. Finally, the device was patterned to

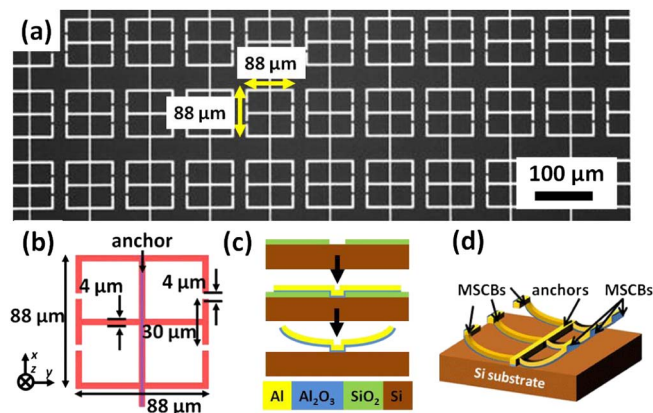


Fig. 1. (a) SEM image of eSRR array. (b) Dimensions of unit cell in layout. (c) Fabrication process flow of eSRR-MSCBs. (d) Schematic diagram of eSRR-MSCBs after microstructures are released.

open etching holes for releasing the structures. Then vapor hydrogen fluoride (VHF) was applied to release the MSCBs. Figure 1(d) shows the 3D schematic diagram of the MSCBs, which were connected to the anchor and can be simultaneously actuated downward from the original bending position (up state) to the snap-down position (down state). The eSRR-MSCBs have two inductive loops connected in parallel, in which the resonant frequency of the circuit model is  $\omega_{LC} = 1/\sqrt{LC} = (c_0/l\sqrt{\epsilon_C})\sqrt{d/w}$ . Here,  $C = \epsilon_0\epsilon_C wt/d$  and  $L = \mu_0 l^2/t$  are used for calculating the respective capacitance and inductance of the gap within the eSRR, where  $c_0$  is the velocity of light in vacuum,  $w$  is the width of metal,  $d$  is the width of capacitor gap,  $t$  is the metal thickness,  $l$  is the size of the eSRR,  $\epsilon_0$  is the free space permittivity, and  $\epsilon_C$  is the relative permittivity of the materials in the capacitor gap [18]. A resonator was designed with four capacitor plates (the splits) which couple strongly to the electric field, while the inductive element (the frames of the loops) does not. Tunability of the resonant frequency of the eSRR-MSCBs can be achieved by replacing the fixed capacitor with six flexible cantilever beams; that is, the adjustable deflected shape of the cantilever beams will modify the capacitor.

The MSCBs curl upward because the  $\text{Al}_2\text{O}_3$  is under compressive residual stress while the Al film is under tensile residual stress. To actuate the MSCBs, a voltage is applied between the MSCBs and the substrate. Electrostatic force lowers the MSCBs from the up state to the down state. In Fig. 2, the radius of curvature and bending height of MSCBs as a function of Al layer thickness is expressed by the equation [19]

$$\frac{1}{R} = \frac{\Delta T \cdot (\alpha_2 - \alpha_1)}{\frac{t_1 + t_2}{2} + \frac{2(E_1 I_1 + E_2 I_2)}{t_1 + t_2} \cdot \left( \frac{1}{E_1 t_1} + \frac{1}{E_2 t_2} \right)}, \quad R \propto t_2, \quad (1)$$

where subscripts 1 and 2 refer to  $\text{Al}_2\text{O}_3$  and Al materials, respectively;  $t$  is the thickness of thin films ( $t_1 = 20$  nm and  $t_2 = 500$  nm);  $E$  is the Young's modulus ( $E_1 = 530$  GPa and  $E_2 = 70$  GPa);  $\alpha$  is the coefficient of thermal expansion ( $\alpha_1 = 8.1 \times 10^{-6} \text{ K}^{-1}$ ,  $\alpha_2 = 23.1 \times 10^{-6} \text{ K}^{-1}$ );  $I$  is the area moment of inertia;  $A$  is the area of curved beam; and  $\Delta T$  is the temperature difference within the fabrication process. After the eSRR-MSCB

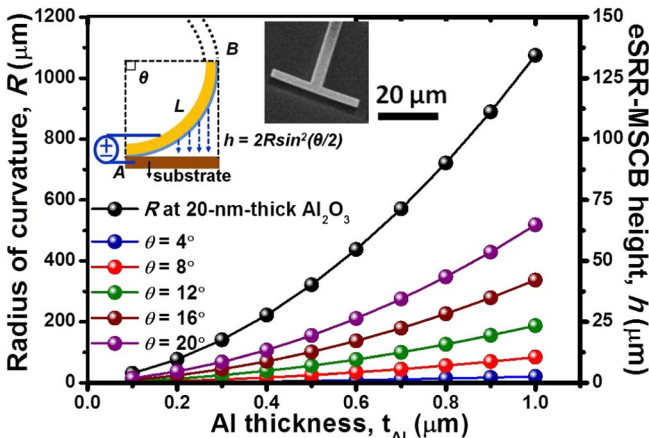


Fig. 2. Radius of curvature and bending height of eSRR-MSCBs as a function of layer thickness.

device is released by VHF, the bending height of the stressed beam is given by the equation  $h = 2R \sin^2(\theta/2) \propto R \propto t_2$ . The radius of curvature and bending height are proportional to the thickness of the Al layer. This indicates that the MSCBs which have a thicker Al layer can achieve larger radius of curvature. The inset of Fig. 2 shows the schematic drawing of curved beams. The cantilever beam will be curved extremely if  $\theta$  is exceeded  $90^\circ$ . Because the effective electrostatic force on AB is dominated than the one extremely curved on the top of AB, the  $\theta$  is within the range of  $0 \sim 90^\circ$  can effectively contribute on the electrostatic force. Thus, the maximum bending height of the cantilever beam is considered as  $R$ . Here, we chose the thickness of the Al layer to be 500 nm. The inset SEM image of Fig. 2 shows the radius of curvature of MSCBs and bending height are 320 and 8  $\mu\text{m}$ , respectively, which are comparable with the modeling results.

To understand the optical properties of the device, 3D finite difference time domain (FDTD) calculations were carried out using software package FDTD solutions to calculate the transmission spectra and the entire electric and magnetic field strength distribution. Figure 3 shows the simulated (red curves) and measured (black curves) transmission spectra of eSRR-MSCBs at 0, 5, and 10 V DC bias, respectively, for both TE and TM polarized incidence. Those transmission spectra were extrapolated and normalized from the ratio of the Fourier-transformed amplitude spectra of the sample to the reference, which is a blank slab identical to the substrate. A terahertz time domain spectroscopy was employed for the optical characterization of the fabricated 3D movable MMs when the gap between the eSRR-MSCBs and the substrate changes. In Figs. 3(a)–3(c), there is one resonant peak being transmitted through the eSRR-MSCBs. The spectral peak was shifted from 0.51 THz [Fig. 3(a)] via 0.63 THz [Fig. 3(b)] to 0.73 THz [Fig. 3(c)] when actuated from

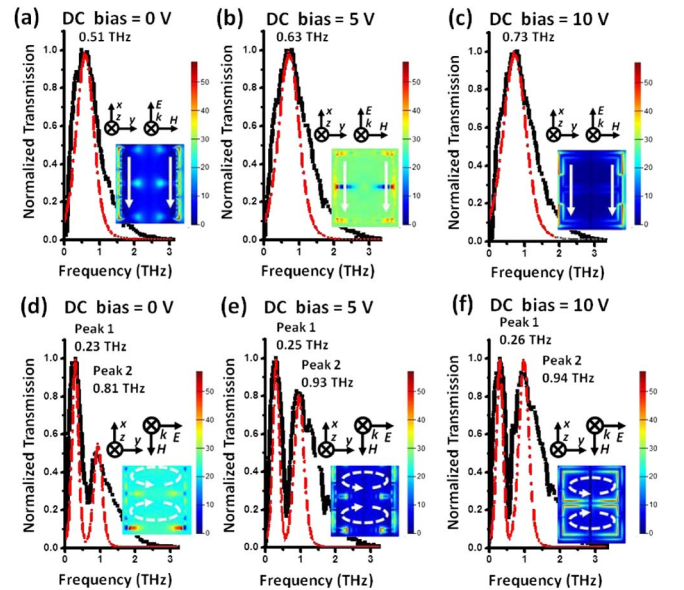


Fig. 3. Simulated (red curves) and measured (black curves) results of eSRR-MSCBs for (a) through (c) TM and (d) through (f) TE polarized incidence at 0, 5, and 10 V DC bias, respectively.

initial state (0 V DC bias) to downward states (5 and 10 V DC bias). The electric field is along the  $x$  direction and the corresponding electric field distributions are shown in the inset of Figs. 3(a)–3(c). The spectrum of the device has one resonant peak due to the electric field that is perpendicular to the four capacitor plates being coupled to the capacitive elements, which resulted in a transmission peak. On the contrary, the TE polarized incidence has two resonant peaks as shown in Figs. 3(d)–3(f). The two resonant peaks of eSRR-MSCBs were blue-shifted by 0.03 THz (peak 1) and 0.13 THz (peak 2) when compared with the device without driving voltage [0 V DC bias, Fig. 3(d)] to pull-in voltage [10 V DV bias, Fig. 3(f)]. That electric field is along the  $y$  direction while the corresponding electric field distributions are shown in the inset of Figs. 3(d)–3(f). These two resonant peaks are originated from these two current loops. This indicates that reconfigurable and movable 3D MMs can be achieved by adjusting the gap between the MSCBs and substrate. Such tunable ranges for TM and TE polarized incidence are 0.22 and 0.13 THz, respectively. They are comparable with those reported in literature that used MEMS-based MMs [10–13] but did not effectively overcome the limitations by means of semiconductor diodes [5,6] and liquid crystal [8,9] owing to the air gap of eSRR-MSCBs between the metallic structures and the substrate not being large enough. The effective improvement method can increase the thickness of the Al or Al<sub>2</sub>O<sub>3</sub> layer for larger bending height of MSCBs referred to in the modeling results in Fig. 2. Furthermore, the intensity ratio of the first and second resonant frequency of eSRR-MSCBs for TE polarized incidence is increased 2.50-fold and 1.25-fold operated at 10 V DC bias compared to the device without and 5 V DC bias, respectively. The first and second resonant frequency of eSRR-MSCBs can be shifted from 0.23 to 0.26 THz and 0.81 to 0.94 THz; that is, the tuning range is 0.03 and 0.13 THz for the first and second peak, respectively.

In conclusion, a 3D movable MM is demonstrated along with active control of tunable THz filter by using MSCBs to adjust the gap between metallic eSRR structures and substrate. Although the tuning range of resonant peaks for TM and TE polarized incidence are only 0.22 and 0.13 THz, respectively, the variation of first and second peaks for transmission intensity at TE mode is enhanced 2.50-fold. This device will not only promise practical applications in polarization control of light, but it may also be implemented in optical filter and sensor applications. The optimization of 3D movable MMs at specific wavelengths can be made based on the relation of capacitance and inductance, which are proportional to the size of MMs. Furthermore, the large radius of

curvature and small gap between MSCBs and substrate resulted in small driving DC bias. However, the small gap will restrict the tunable range of eSRR-MSCBs, resulting in a trade-off between the driving voltage and tunable range of eSRR-MSCBs. Therefore, an optimized design with desirable operation voltage, that is, DC bias, and enlarged tuning range could be conceptualized and developed upon the application needs in the future.

This work was supported by MOE2012-T2-2-154 (Monolithic Integrated Si/AlN Nanophotonics Platform for Optical NEMS and OEICs) under WBS No. R-263-000-A59-112.

## References

1. H. J. Lezec, J. A. Dionne, and H. A. Atwater, *Science* **316**, 430 (2007).
2. J. Valentine, S. Zhang, T. Zentgraf, E. Ulin-Avila, D. A. Genov, G. Bartal, and X. Zhang, *Nature* **455**, 376 (2008).
3. G. Dolling, C. Enkrich, M. Wegener, C. M. Soukoulis, and S. Linden, *Opt. Lett.* **31**, 1800 (2006).
4. X. Wang, Y.-H. Ye, C. Zheng, Y. Qin, and T. J. Chi, *Opt. Lett.* **34**, 3568 (2009).
5. O. Paul, C. Imhof, B. Lagel, S. Wolff, J. Heinrich, S. Hofling, A. Forchel, R. Zengerle, R. Beigang, and M. Rahm, *Opt. Express* **17**, 819 (2009).
6. Y. C. Jun and I. Brener, *J. Opt.* **14**, 114013 (2012).
7. L. Kang, Q. Zhao, H. J. Zhao, and J. Zhou, *Opt. Express* **16**, 8825 (2008).
8. Z. Liu, C. Y. Huang, H. Liu, X. Zhang, and C. Lee, *Opt. Express* **21**, 6519 (2013).
9. F. Zhang, Q. Zhao, W. Zhang, J. Sun, J. Zhou, and D. Lippens, *Appl. Phys. Lett.* **97**, 134103 (2010).
10. H. Tao, A. C. Strikwerda, K. Fan, W. J. Padilla, X. Zhang, and R. D. Averitt, *Phys. Rev. Lett.* **103**, 147401 (2009).
11. W. M. Zhu, A. Q. Liu, X. M. Zhang, D. P. Tsai, T. Bourouina, J. H. Teng, X. H. Zhang, H. C. Guo, H. Tanoto, T. Mei, G. Q. Lo, and D. L. Kwong, *Adv. Mat.* **23**, 1792 (2011).
12. W. M. Zhu, A. Q. Liu, W. Zhang, J. F. Tao, T. Bourouina, J. H. Teng, X. H. Zhang, Q. Y. Wu, H. Tanoto, H. C. Guo, G. Q. Lo, and D. L. Kwong, *Appl. Phys. Lett.* **99**, 221102 (2011).
13. W. M. Zhu, A. Q. Liu, T. Bourouina, D. P. Tsai, J. H. Teng, X. H. Zhang, G. Q. Lo, D. L. Kwong, and N. I. Zheludev, *Nat. Commun.* **3**, 1274 (2012).
14. N. R. Han, Z. C. Chen, C. S. Lim, B. Ng, and M. H. Hong, *Opt. Express* **19**, 6990 (2011).
15. X. Li, L. Yang, C. Hu, X. Luo, and M. Hong, *Opt. Express* **19**, 5283 (2011).
16. Z. C. Chen, R. Mohsen, Y. D. Gong, T. C. Chong, and M. H. Hong, *Adv. Mater.* **24**, OP143 (2012).
17. N. I. Zheludev, *Science* **328**, 582 (2010).
18. C. M. Soukoulis, M. Kafesaki, and E. N. Economou, *Adv. Mater.* **18**, 1941 (2006).
19. M. Shavezipur, W. Guo, C. Carraro, and R. Maboudian, *J. Microelectromech. Syst.* **21**, 541 (2012).